Research Article Vol. 5, No. 6 / June 2018 / Optica 733

Coded cone-beam x-ray diffraction tomography with a low-brilliance tabletop source

Zheyuan Zhu, Ryan A. Ellis, and Shuo Pang*

CREOL, The College of Optics and Photonics, University of Central Florida, 4304 Scorpius St, Orlando, Florida 32816, USA
*Corresponding author: pang@creol.ucf.edu

Received 16 January 2018; revised 23 March 2018; accepted 25 April 2018 (Doc. ID 319992); published 5 June 2018

X-ray diffraction tomography (XDT) probes the spatially variant x-ray diffraction (XRD) profile within volumetric objects. Here, we demonstrate a tabletop XDT setup with coded cone-beam illumination that accelerates the acquisition process of three-dimensional (3D) objects. Compared to the attenuation-based x-ray computed tomography (CT), XDT images display high contrast and specificity among materials with similar absorption coefficients. However, due to the weak signal level of diffraction and the low efficiency in source utilization and detection, conventional XDT systems require high-brilliance synchrotron sources to manage the acquisition time. In this paper, we propose a coded-illumination XDT system that utilizes the cone-beam from a tabletop x-ray tube and eliminates the detector-side collimation. The multiplexed measurement promotes parallelization in the data acquisition and enables simple implementation of compressive measurements, addressing the need of tabletop XDT systems in industrial nondestructive testing and medical imaging applications. We have demonstrated 1 order of magnitude reduction in XDT acquisition time, making high-contrast 3D x-ray imaging accessible to various research and application areas.

OCIS codes: (110.7440) X-ray imaging; (110.6960) Tomography; (170.1630) Coded aperture imaging; (110.1758) Computational imaging.

https://doi.org/10.1364/OPTICA.5.000733

1. INTRODUCTION

X-ray computed tomography (CT) is an indispensable volumetric imaging tool in medical and industrial imaging settings. The contrast of attenuation-based CT images among biological soft tissues, liquids, or polymer composites, however, is insignificant, due to their similar electron densities. Because of the high penetration depth of x rays, x-ray diffraction (XRD) is an ideal module for analyzing subnanometer scale structure of bulk objects and has been widely applied in material phase identification, domain mapping of polycrystals, and nondestructive strain and stress imaging [1–6]. The material-specific XRD signature enables the detection of dilute substances under the concentration as low as one part per thousand [7,8] and has shown its potential in increasing the sensitivity and specificity for biomedical and security screening applications [9–12]. By translating a pencil x-ray beam across a sample to capture the diffraction patterns at each location, scanning small- and wide-angle x-ray scattering (scanning SWAXS) imaging [13,14] obtains a two-dimensional (2D) material map, but does not resolve the depth information.

Acquiring the XRD profile within a three-dimensional (3D) object entails decoupling the location of the scatter along the illumination beam. This can be accomplished via coded aperture on either the illumination side [15,16] or detector side [17,18], but the resulting depth resolution is ∼10 times worse than the transverse resolution, due to the small diffraction angle. To improve the depth resolution, tomographic setups that combine scanning x-ray scattering measurement with sample rotation similar to that in CT have been demonstrated, such as x-ray diffraction tomography (XDT) [10,19] and small-angle x-ray scattering (SAXS) tomography [4,14,20]. However, these setups typically require the incident x ray to be reduced to a narrow pencil beam, resulting in a low utilization efficiency of the source. This spatial filtration, combined with the intrinsically small XRD cross section, necessitates either tens of hours in acquisition time, or a high-brilliance synchrotron source [4,7,10,14]. A fast, volumetric XDT system using a commercially available x-ray tube is thus desirable in real-life applications.

Throughout the history of CT evolution, projection parallelization has played a vital role in accelerating the scan speed: from several minutes for one slice by pencil-beam CT [21], to less than 1 min for the full volume by cone-beam CT [22]. However, unlike CT evolution [Figs. 1(a) and 1(b)], parallelizing conventional XDT measurement requires additional detector-side collimators to distinguish the XRD signal from individual beams. Fan-beam XDT, also known as coherent scattering computed tomography (CSCT) [23,24], opens up the illumination to the fan beam, yet requires one-dimensional (1D) collimation on the detector side [Fig. 1(c)], compromising the efficiency in detection. Further development from fan-beam to cone-beam geometry has faced an obstacle in finding the correct detection scheme for cone-beam parallelization [25]: XDT with a direct cone-beam illumination [Fig. 1(d)] would fail to reconstruct 3D objects due to the overlapping of the diffracted photons from different vertical layers.

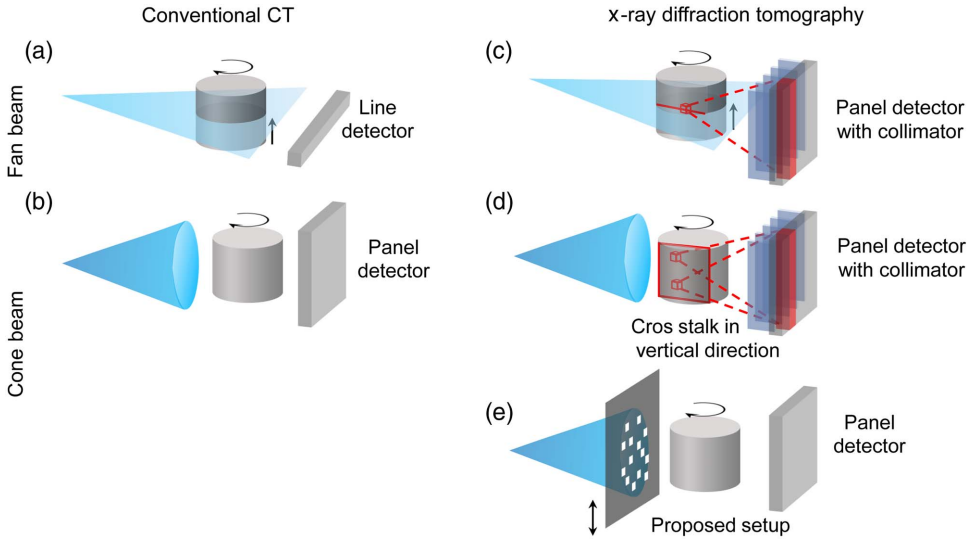

Fig. 1. Comparison between CT and XDT systems. (a) Fan-beam CT; (b) cone-beam CT, which opens up fan-beam to cone-beam illumination and uses a panel detector to capture 2D radiographies; (c) fan-beam XDT (or CSCT). Detector-side collimators are required to localize the scattering volume. (d) Opening up fan-beam to cone-beam cannot further parallelize the XDT measurement, because the scattering signal from different layers will overlap on the detector. (e) Our proposed cone-beam setup with illumination coding allows volumetric imaging with high collection efficiency. The scattering signal from each beam can be retrieved by changing the illumination pattern.

This work aims at developing a fast, volumetric XDT imaging system with a low brilliance, tabletop x-ray source. We introduce a cone-beam multiplexing scheme tailored for projection measurement in volumetric XDT [Fig. 1(e)]. Compared to pencil-beam XDT, the coded illumination improves the utilization of the cone beam, thus increasing the XRD signal to background noise ratio. By switching the illumination pattern on the mask, XRD signals associated with individual beams can be retrieved without using a detector-side collimator. In addition, the illumination-coded cone-beam XDT setup also facilitates the integration of a compressive tomography scheme [26] that further accelerates the image acquisition process. Compared to the conventional XDT, our system achieves high efficiency on illumination and detection and reduces the imaging time by ∼10 times.

2. IMAGING PRINCIPLE

In the coded illumination XDT setup, a mask is placed after the shaped cone beam to modulate the illumination pattern on the sample. The scattering signal from the sample is directly collected by a panel detector to maximize collection efficiency. Figure 2 compares the geometry of our setup with a conventional pencil-beam XDT. A single pinhole mask would reduce the system to a pencil-beam XDT setup [Fig. 2(a)], in which the 2D diffraction pattern is a superposition of diffraction signal from the voxels along the pencil beam. Under small diffraction angle, the interaction between incident photon and the sample is dominated by coherent scattering [19], whose intensity is described by

$$dI = I_0 \frac{r_e^2}{2}(1+\cos^2\theta) f(\mathbf{r}, q) d\Omega dV dq, \tag{1}$$

where I_0 is the irradiance of the narrowband source, r_e is the classical electron radius, θ is the angle between incident and diffracted beam, $d\Omega$ is the solid angle covered by the detector pixel, the scattering volume $dV = Adt$, where A is the cross-section area of the beam, and t is the depth coordinates along the pencil beam. The four-dimensional (4D) object is expressed in the spatial (3D) and momentum transfer (1D) domain $f(\mathbf{r}, q) = n(\mathbf{r})F^2(\mathbf{r}, q)$, which is the product between the density of scattering material $n(\mathbf{r})$ and the square of molecular form factor $F(\mathbf{r}, q)$.

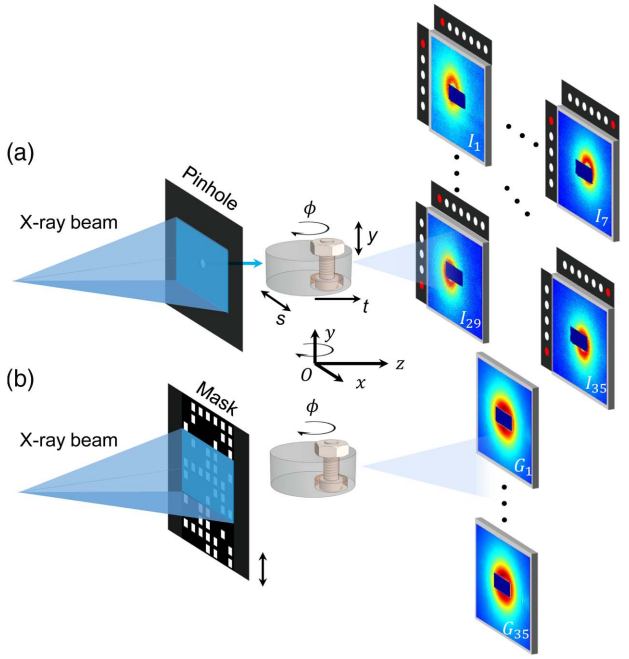

Fig. 2. Pencil-beam and multiplexed XDT geometry. (a) Pencil-beam XDT. The red dot above each scattering pattern indicates which pinhole along the row (y direction) and column (s direction) generates this diffraction image. (b) XDT with illumination coding. The illumination pattern is changed by shifting the mask vertically. The individual scattering pattern generated by each pencil beam can be retrieved from these measurements.

The momentum transfer q that causes the deviation of photons with energy E and scattering angle θ is defined by Bragg's law and can be approximated under small angle

$$q = \frac{E}{hc}\sin\left(\frac{\theta}{2}\right) = \frac{E}{hc}\frac{w}{2(L-t)}, \tag{2}$$

where w is the distance between the detector pixel and the pencil beam, L is the distance between the rotation center and the detector plane, h is the Planck constant, and c is the speed of light. Equation (2) establishes the dependence of the momentum transfer, q, on the position of the scatter along the beam, t. The forward and back projection are both performed along a family of curves in q-t space [27] (Section 1B in Supplement 1). To resolve the scattering profile from each voxel within a 3D volume in this pencil-beam geometry, the sample needs to be translated along both the x and y directions and rotated around the y direction.

The multiplexing scheme in our cone-beam illumination-coded XDT opens up multiple pinholes on the mask to create an array of pencil beams illuminating the sample, as shown in Fig. 2(b). Let us denote the 2D diffraction pattern under ith illumination pattern by $G_i(x_d, y_d)$, where x_d, and y_d are the coordinates of the detector pixels. The multiplexed diffraction pattern can be expressed as a superposition of $I_j(x_d, y_d)$, the diffraction pattern generated by individual pencil-beam j:

$$G_i(x_d, y_d) = \sum_j S_{ij} I_j(x_d, y_d), \tag{3}$$

where S_{ij} is the matrix element that stores the weight of each individual diffraction pattern. The scattering intensity from an individual pencil beam can be recovered from the measurement by inversing the matrix $\mathbf{S}$. Considering the practical constraints that the matrix element is in the range $0 \le S_{ij} \le 1$, the S-matrix was adopted to maximize the signal-to-noise ratio (SNR) of the measurement [28]. In our experiment, we divided the illumination into an array of 35 beams and chose $\mathbf{S}_{35}$, with 0 and 1 entries corresponding to either blocking or opening the jth pencil beam. To optimize the physical size and minimize the translation of the illumination mask, we applied the cyclic construction of $\mathbf{S}_{35}$ by folding each row of the $\mathbf{S}_{35}$ matrix into a 5 by 7 2D array. Thirty-five different illumination patterns were created in the experiment by stepping the mask one row at a time along the vertical direction. Figure 3 shows two mask designs according to $\mathbf{S}_{35}$, one for normal Hadamard multiplexing scheme [(a1), (a2)], and the other for multiplexing with compression [(a3), (a4)].

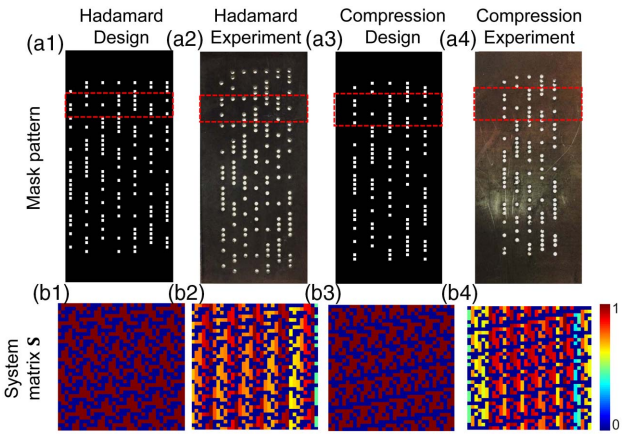

Fig. 3. Binary Hadamard mask designed (a1) and manufactured (a2) according to $\mathbf{S}_{35}$. Designed (a3) and manufactured (a4) Hadamard mask for compression according to $\mathbf{S}_{35}$. (b1)–(b4) System matrix corresponding to each mask. The red, dashed rectangle marks the size of the shaped beam on the mask.

3. MATERIALS AND METHODS

The pattern of the mask was fabricated on a 1/16 inch thick lead sheet by a milling machine. The diameter of each pinhole on the mask is 1 mm, and the vertical pitch between adjacent rows is 1.4 mm. For the normal Hadamard mask, each illumination pattern consists of seven columns with 3 mm horizontal pitch and covers five vertical sample layers. Under each projection, the sample was translated by three steps horizontally to fill in the gaps between the pinholes. For the Hadamard mask designed for compressive tomography, each illumination pattern consists of five columns with a 4 mm horizontal pitch and covers seven vertical sample layers. Instead of scanning the sample continuously across the mask to fill in the illumination gap, the sample was positioned to a random horizontal location under each projection. Figure 3(a) shows a photo of the manufactured mask. The system matrix of the mask was calibrated using a homogenous scatter to compensate for the nonuniform illumination on each pinhole (Section 2 in Supplement 1), as shown in Fig. 3(b). The XDT setup employs a copper-anode x-ray tube (XRT 60, Proto Manufacturing), operating under 45 kV and 40 mA. The x-ray focus size was 0.8 mm. The sample was mounted on a rotation stage (RV1200P, Newport) to capture projections over 180° at a step size of 6°. The distance between the x-ray focus and the mask was 260 mm, and that between the mask and the object was 40 mm. Each pencil beam created by this collimation geometry was 1 mm in diameter and had a divergence angle of ~0.17°. The cone angle of the illumination over the whole sample was 1.3°. A linear stage (UTM150CC, Newport) moved the mask vertically to change the pattern of coded illumination. The scattered x rays from the sample were captured by a flat panel detector (1215CF-MP, Rayence). To block the transmitted x ray, a lead beam stop with a size of 25 mm by 10 mm was placed at the center of the detector. The distance between the detector plane and the rotation center was 170 mm. The effective pixel size on the detector was 200 μm by 200 μm after 4 by 4 binning.

To experimentally demonstrate the illumination-encoded XDT, a sample consisting of a circular piece of acrylic and a #8–32 nylon screw was imaged by the setup. The acrylic piece is 10 mm thick and has a 1/8 inch hole drilled at an off-center position. The screw was secured by a washer and a nut, both of which were made of nylon. A reconstructed CT projection of the sample is shown in Fig. 4(c). For XDT image acquisition, the integration time for each diffraction pattern was 15 s, resulting in an average of ~1500 pixel value at the scattering peak. To image all 14 layers, the sample was translated vertically by three 7 mm steps under the Hadamard mask, and two 9.8 mm steps under the Hadamard mask with compression. The total imaging time for a volume size [21 mm (L) by 21 mm (W) by 19.6 mm (H)] was 45 h using the Hadamard mask, and 10 h using the Hadamard mask with compressive measurement. Diffraction profiles of acrylic and nylon were also recorded for reference. Two 1 mm thick parallel slabs of both materials were placed directly under a 1 mm pencil beam with an integration time of 30 s.

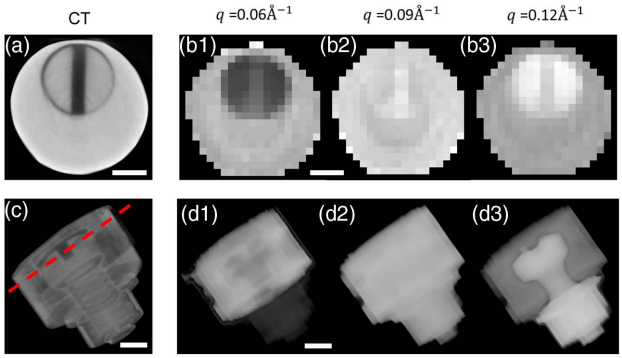

Fig. 4. CT and XDT reconstruction of the sample. (a) CT image of the layer marked by the red, dashed line in (c). (b) XDT reconstruction at $q = 0.06$, 0.09, and 0.12 Å, respectively. (c) 3D rendering of the attenuation map of the sample. (d) 3D rendering of XDT reconstruction on all sample layers at $q = 0.06$, 0.09, and 0.12 Å (Visualization 1). All scale bars represent 5 mm.

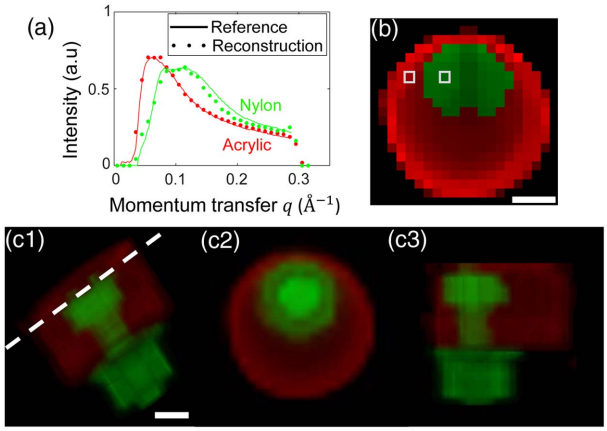

Fig. 5. Material identification based on the XDT reconstruction. (a) Reconstructed form factor of the acrylic and nylon from two representative pixels marked in (b) compared with references. (b) Material map of the layer marked by the white, dashed line in (c). Acrylic and nylon are rendered in red and green, respectively. (c) 3D rendering of the material map from different perspectives. All scale bars represent 5 mm.

For a given rotation angle, the 35 images $\mathbf{G} = (G_1 \ldots G_{35})$ captured under the multiplexed illumination patterns were first decomposed into the diffraction patterns from individual pinhole $\mathbf{I} = (I_1 \ldots I_{35})$ by inverting the calibrated system matrix $\mathbf{S}$. Each diffraction pattern was then azimuthally integrated to obtain the intensity profile along the radial direction, w. Given the location of each pinhole, the measurement was regrouped into a series of high-dimensional sinograms $I(s, \phi; w, y)$ at each radial position w on layer y and corrected by the CT transmission data of the corresponding layer to compensate for the absorption of the sample [29]. Finally, an individual vertical layer was reconstructed using the 2D angular-dispersive XDT reconstruction [27] (Section 3A in Supplement 1).

4. RESULTS AND DISCUSSION

A. Multiplexing XDT Reconstruction Results

The 4D object reconstruction is sampled at 1 mm^3 in spatial domain and 0.01 $Å^{-1}$ in the momentum transfer domain. Figure 4 shows the reconstructed object from the Hadamard mask [Fig. 3(a2)]. Figures 4(b1)–4(b3) and 4(d1)–4(d3) display the 2D and 3D spatial profile reconstructed at $q = 0.06$, 0.09, and 0.12 $Å^{-1}$. The background is less than 10% of the reconstructed peak diffraction intensity. The CT reconstruction [Fig. 4(a)] has an average gray-scale value of 0.77 ± 0.06 and 0.63 ± 0.04 (normalized to the maximum) for acrylic and nylon. The x-ray attenuation image shows poor contrast between the two polymer materials because of their similar electron densities. For XDT reconstruction, the average gray-scale values for acrylic and nylon are 0.71 ± 0.04 and 0.36 ± 0.09 at $q = 0.06$ $Å^{-1}$, and 0.70 ± 0.03 and 0.92 ± 0.06 at $q = 0.12$ $Å^{-1}$. The high contrast between the two materials in the XRD image reveals the differences in molecular compositions and structural arrangements.

Figure 5(a) compares the reconstructed coherent scattering form factor of acrylic and nylon [marked by the red and green pixels in (b)] with the experimentally measured reference profile. The reconstructed XRD profile of acrylic has a peak around 0.05 $Å^{-1}$, and that of nylon exhibits a broad peak around 0.1 $Å^{-1}$. Considering the worst momentum transfer resolution, 0.01 $Å^{-1}$, of the system (Section 4A in Supplement 1), the shapes and peak locations of both materials are consistent with previously reported results [30]. The normalized mean square difference between the reconstruction and reference is 1.8% for acrylic and 1.1% for nylon. This consistency allows us to perform material identification with high specificity based on the momentum transfer domain of the reconstructed 4D object. The material of each voxel can be identified by matching the reconstructed scattering form factor with the references in angular metric (Section 3B in Supplement 1). Figure 5(b) shows the material map of the layer marked by the white, dashed line in Fig. 5(c), with acrylic rendered in red, nylon rendered in green. Figure 5(c) displays the material of each voxel within the sample volume under three different perspectives.

B. Comparison with Existing XDT Systems

The reconstruction from our system is verified by a pencil-beam XDT scan under equivalent experimental parameters. We replaced the mask with a 1 mm pinhole and translated the sample across the beam in 21 steps, which are equivalent to the full horizontal resolution in our multiplexed scheme. The sample was rotated every 6° for 180° to capture the same number of projections as in the multiplexed scheme. The integration time for each scattering pattern was 30 s, and the total acquisition time for one sample layer was 6 h.

Our system facilitates the integration of compressive tomography in the measurement to further reduce the imaging time. Figure 6 compares the reconstruction of one sample layer, located at 5.6 mm below the top of the sample, from the normal Hadamard mask [Fig. 3(a2)], the Hadamard mask with compression [Fig. 3(a4)], and conventional pencil-beam XDT. In terms of the spatial profile and material contrast, all three schemes produce consistent results. Compared with pencil-beam XDT, the mean square difference of the reconstructed XRD profiles, quantified by normalized mean-square error, is 0.8% for nylon and 1.2% for acrylic for the multiplexing scheme, and 2.1% for nylon and 2.3% for acrylic for the compression scheme. To ensure the same beam divergence emerging from the pinhole array, the mask

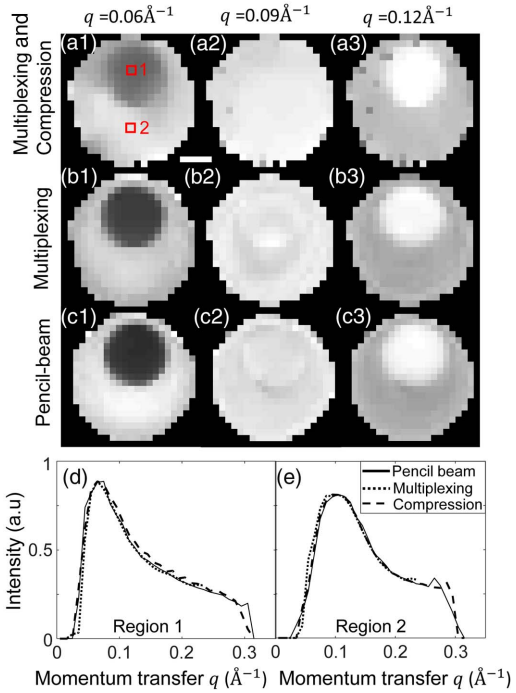

Fig. 6. Reconstruction comparison of the Hadamard multiplexing scheme, Hadamard multiplexing with compression scheme, and pencil-beam XDT (layer located at 5.6 mm from the sample top). (a) Reconstruction from Hadamard mask with compressive tomography at $q = 0.06$, 0.09, and 0.12 Å^{-1}, respectively. The scale bar represents 5 mm. (b) Reconstruction from the full projection data measured using a normal Hadamard mask at the same q values; (c) reconstruction from the pencil-beam XDT scan; (d), (e) comparison between the reconstructed form factors with the reference profile for the pixels marked by red (acrylic region) and green (nylon region), respectively.

designed for compressive measurement, which illuminates seven sample layers at a time, has to be placed farther away from the x-ray focus than the normal Hadamard mask, thus lowering the photon flux on the sample. The slight increase in the reconstruction error could be a result of weaker illumination intensity in the compressive tomography setup.

The multiplexing scheme eliminates the detector-side collimation, simplifies the system setup, and increases the collection solid angle by ~170 times compared to that of fan-beam XDT [24]. The improved detection efficiency unlocks the opportunities for radiation dose-sensitive applications, such as medical imaging. In addition, the multiplexing scheme opens the full cone beam of a tabletop x-ray tube, improving the utilization efficiency of the source.

Compared to the pencil-beam setup, the noise of the measurement determines the gain in acquisition speed of the multiplexing scheme. The noise from our detection system can be modeled as a combination of Poisson and Gaussian noise [31]. If the pencil-beam XDT scan were performed on the entire sample [21 mm (L) by 21 mm (W) by 19.6 mm (H)] under the current noise model, the total imaging time would be 98 h to maintain the same SNR (Section 4B in Supplement 1). With an imaging time of 10 h, the compression scheme achieves 9.8 times faster imaging speed and comparable reconstruction quality as pencil-beam XDT. For fan-beam XDT systems, despite the parallelization in the projection measurement, the detector collimator compromises the collection efficiency, and similar imaging time as pencil-beam XDT would be required to obtain the same SNR in reconstruction.

It is worth noting that our imaging scheme is suitable for a high spatial resolution setup. The demonstrated resolution is determined by the size of each pinhole, which is ~1 mm. In conventional XDT, the resolution relies on the size of the pinhole or the collection angle of the collimators. A high spatial resolution system would yield a lower efficiency. Since our illumination mask has a ~50% utilization of the cone beam, using a higher-order Hadamard mask with smaller feature size can improve the spatial resolution without sacrificing the source utilization efficiency. The SNR improvement of a cyclic Hadamard code is proportional to $\sqrt{N/4}$, where N is the number of multiplexed beams [28]; if the same sample were imaged under a spatial resolution of 0.1 mm, the coded illumination scheme alone would achieve ~100 times reduction in imaging time compared to a pencil-beam XDT.

5. CONCLUSION

In summary, we have demonstrated a tabletop XDT system that reconstructs the molecular form factor of 3D objects. The XRD image provides high contrast among samples with similar electron density but different molecular composition, allowing the material of each voxel within the sample to be identified according to the XRD profile. The illumination coding simultaneously accomplishes high efficiency on both the source and detector side. Our compressive, multiplexed XDT system has demonstrated 1 order of magnitude reduction in imaging time. The gain in acquisition speed becomes more significant in high-resolution imaging. Similar to the evolution in conventional CT [25], the coded illumination method promotes parallelization in volumetric XRD imaging, reducing the imaging time for a tabletop XDT system.

Our coded illumination XDT scheme is compatible with existing CT scanners. The switching of illumination pattern can be implemented by translating the object on a conveyer belt with a stationary mask [32], thus enabling the XDT as a high-specificity secondary scan module in a cone-beam CT scanner, which can potentially improve the sensitivity in medical diagnostics and *in situ* material characterization.

Funding. National Science Foundation (NSF) (DMS-1615124).

See Supplement 1 for supporting content.

REFERENCES

1. J. D. Budai, W. Yang, N. Tamura, J.-S. Chung, J. Z. Tischler, B. C. Larson, G. E. Ice, C. Park, and D. P. Norton, "X-ray microdiffraction study of growth modes and crystallographic tilts in oxide films on metal substrates," Nat. Mater. **2**, 487–492 (2003).
2. W. Ludwig, E. M. Lauridsen, S. Schmidt, H. F. Poulsen, and J. Baruchel, "High-resolution three-dimensional mapping of individual grains in polycrystals by topotomography," J. Appl. Crystallogr. **40**, 905–911 (2007).
3. P. Reischig, A. King, L. Nervo, N. Viganó, Y. Guilhem, W. J. Palenstijn, K. J. Batenburg, M. Preuss, and W. Ludwig, "Advances in X-ray diffraction contrast tomography: flexibility in the setup geometry and application to multiphase materials," J. Appl. Crystallogr. **46**, 297–311 (2013).
4. F. Schaff, M. Bech, P. Zaslansky, C. Jud, M. Liebi, M. Guizar-Sicairos, and F. Pfeiffer, "Six-dimensional real and reciprocal space small-angle X-ray scattering tomography," Nature **527**, 353–356 (2015).

5. M. A. Pfeifer, G. J. Williams, I. A. Vartanyants, R. Harder, and I. K. Robinson, "Three-dimensional mapping of a deformation field inside a nanocrystal," Nature **442**, 63–66 (2006).
6. I. Robinson and R. Harder, "Coherent X-ray diffraction imaging of strain at the nanoscale," Nat. Mater. **8**, 291–298 (2009).
7. P. Bleuet, E. Welcomme, E. Dooryhée, J. Susini, J.-L. Hodeau, and P. Walter, "Probing the structure of heterogeneous diluted materials by diffraction tomography," Nat. Mater. **7**, 468–472 (2008).
8. S. Huotari, T. Pylkkänen, R. Verbeni, G. Monaco, and K. Hämäläinen, "Direct tomography with chemical-bond contrast," Nat. Mater. **10**, 489–493 (2011).
9. Z. Zhu, A. Katsevich, A. J. Kapadia, J. A. Greenberg, and S. Pang, "X-ray diffraction tomography with limited projection information," Sci. Rep. **8**, 522 (2018).
10. U. Kleuker, P. Suortti, W. Weyrich, and P. Spanne, "Feasibility study of x-ray diffraction computed tomography for medical imaging," Phys. Med. Biol. **43**, 2911–2923 (1998).
11. H. Strecker, G. L. Harding, H. Bomsdorf, J. Kanzenbach, R. Linde, and G. Martens, "Detection of explosives in airport baggage using coherent x-ray scatter," Proc. SPIE **2092**, 399–410 (1994).
12. G. Harding, "X-ray scatter tomography for explosives detection," Radiat. Phys. Chem. **71**, 869–881 (2004).
13. C. Giannini, D. Siliqi, O. Bunk, A. Beraudi, M. Ladisa, D. Altamura, S. Stea, and F. Baruffaldi, "Correlative light and scanning X-ray scattering microscopy of healthy and pathologic human bone sections," Sci. Rep. **2**, 435 (2012).
14. C. G. Schroer, M. Kuhlmann, S. V. Roth, R. Gehrke, N. Stribeck, A. Almendarez-Camarillo, and B. Lengeler, "Mapping the local nanostructure inside a specimen by tomographic small-angle x-ray scattering," Appl. Phys. Lett. **88**, 164102 (2006).
15. P. Evans, K. Rogers, A. Dicken, S. Godber, and D. Prokopiou, "X-ray diffraction tomography employing an annular beam," Opt. Express **22**, 11930–11944 (2014).
16. A. J. Dicken, J. P. O. Evans, K. D. Rogers, D. Prokopiou, S. X. Godber, and M. Wilson, "Depth resolved snapshot energy-dispersive X-ray diffraction using a conical shell beam," Opt. Express **25**, 21321–21328 (2017).
17. K. MacCabe, K. Krishnamurthy, A. Chawla, D. Marks, E. Samei, and D. Brady, "Pencil beam coded aperture x-ray scatter imaging," Opt. Express **20**, 16310–16320 (2012).
18. K. P. MacCabe, A. D. Holmgren, M. P. Tornai, and D. J. Brady, "Snapshot 2D tomography via coded aperture x-ray scatter imaging," Appl. Opt. **52**, 4582–4589 (2013).
19. G. Harding, J. Kosanetzky, and U. Neitzel, "X-ray-diffraction computed-tomography," Med. Phys. **14**, 515–525 (1987).
20. M. Liebi, M. Georgiadis, A. Menzel, P. Schneider, J. Kohlbrecher, O. Bunk, and M. Guizar-Sicairos, "Nanostructure surveys of macroscopic specimens by small-angle scattering tensor tomography," Nature **527**, 349–352 (2015).
21. G. N. Hounsfield, "Computerized transverse axial scanning (tomography): Part I. Description of system," Br. J. Radiol. **46**, 1016–1022 (1973).
22. A. C. Miracle and S. K. Mukherji, "Conebeam CT of the head and neck, Part 1: physical principles," Am. J. Neuroradiol. **30**, 1088–1095 (2009).
23. A. Harding, J.-P. Schlomka, and G. L. Harding, "Simulations and experimental feasibility study of fan-beam coherent-scatter CT," Proc. SPIE **4786**, 202–209 (2002).
24. J.-P. Schlomka, A. Harding, U. Van Stevendaal, M. Grass, and G. L. Harding, "Coherent scatter computed tomography: a novel medical imaging technique," Proc. SPIE **5030**, 256–265 (2003).
25. G. Harding, "X-ray diffraction imaging—a multi-generational perspective," Appl. Radiat. Isot. **67**, 287–295 (2009).
26. K. Choi and D. J. Brady, "Coded aperture computed tomography," Proc. SPIE **7468**, 74680B (2009).
27. S. Pang, Z. Zhu, G. Wang, and W. Cong, "Small-angle scatter tomography with a photon-counting detector array," Phys. Med. Biol. **61**, 3734–3748 (2016).
28. M. Harwit and N. J. A. Sloane, *Hadamard Transform Optics* (Academic, 1979).
29. G. Harding and J. Kosanetzky, "Elastic scatter computed tomography," Phys. Med. Biol. **30**, 183–186 (1985).
30. U. van Stevendaal, J. P. Schlomka, A. Harding, and M. Grass, "A reconstruction algorithm for coherent scatter computed tomography based on filtered back-projection," Med. Phys. **30**, 2465–2474 (2003).
31. N. Ratner and Y. Y. Schechner, "Illumination multiplexing within fundamental limits," in *IEEE Conference on Computer Vision and Pattern Recognition* (IEEE, 2007), pp. 1–8.
32. S. Pang, M. Hassan, J. Greenberg, A. Holmgren, K. Krishnamurthy, and D. Brady, "Complementary coded apertures for 4-dimensional x-ray coherent scatter imaging," Opt. Express **22**, 22925–22936 (2014).